Bioactive Materials 30 (2023) 1–14

Contents lists available at ScienceDirect

Bioactive Materials

journal homepage: www.keaipublishing.com/en/journals/bioactive-materials

Microfluidic intestinal organoid-on-a-chip uncovers therapeutic targets by recapitulating oxygen dynamics of intestinal IR injury

Jinjian Huang [a], Ziyan Xu [b], Jiao Jiao [c], Zongan Li [d], Sicheng Li [b], Ye Liu [a], Ze Li [b], Guiwen Qu [a], Jie Wu [e], Yun Zhao [e], Kang Chen [b], Jieshou Li [a], Yichang Pan [f,**], Xiuwen Wu [a,b,***], Jianan Ren [a,b,*]

[a] Research Institute of General Surgery, Jinling Hospital, School of Medicine, Southeast University, Nanjing, 210009, China
[b] School of Medicine, Nanjing University, Nanjing, 210093, China
[c] Department of Rehabilitation, The First Affiliated Hospital of Nanjing Medical University, Nanjing, 210029, China
[d] Jiangsu Key Laboratory of 3D Printing Equipment and Manufacturing, NARI School of Electrical and Automation Engineering, Nanjing Normal University, Nanjing, 210042, China
[e] General Clinical Research Center, Nanjing Benq Hospital, Nanjing Medical University, Nanjing, 210019, China
[f] State Key Laboratory of Materials-Oriented Chemical Engineering, College of Chemical Engineering, Nanjing Tech University, Nanjing, 211816, China

ARTICLE INFO

Keywords:
Ionic barrier of ZIF-8
Microfluidics
Organoid-on-a-chip
Oxygen dynamics
Olfm4

ABSTRACT

Increasing evidence demonstrates that mammals have different reactions to hypoxia with varied oxygen dynamic patterns. It takes ~24 h for tri-gas incubator to achieve steady cell hypoxia, which fails to recapitulate ultrafast oxygen dynamics of intestinal ischemia/reperfusion (IR) injury. Inspired from the structure of native intestinal villi, we engineered an intestinal organoid chip embedded with engineered artificial microvessels based on co-axial microfluidic technology by using pH-responsive ZIF-8/sodium alginate scaffold. The chip was featured on: (i) eight times the oxygen exchange efficiency compared with the conventional device, tri-gas incubator, (ii) implantation of intestinal organoid reproducing all types of intestinal epithelial cells, and (iii) bio-responsiveness to hypoxia and reoxygenation (HR) by presenting metabolism disorder, inflammatory reaction, and cell apoptosis. Strikingly, it was found for the first time that Olfactomedin 4 (*Olfm4*) was the most significantly down-regulated gene under a rapid HR condition by sequencing the RNA from the organoids. Mechanistically, OLFM4 played protective functions on HR-induced cell inflammation and tissue damage by inhibiting the NF-kappa B signaling activation, thus it could be used as a therapeutic target. Altogether, this study overcomes the issue of mismatched oxygen dynamics between *in vitro* and *in vivo*, and sets an example of next-generation multisystem-interactive organoid chip for finding precise therapeutic targets of IR injury.

1. Introduction

Intestinal ischemia/reperfusion (IR) injury usually results from thromboembolic or atherothrombotic vaso-occlusive diseases, and it can lead to hypoxia-associated intestinal barrier disorders and flora translocation, eventually causing multiple organ dysfunctions [1]. Despite decades of imaging and medical advances, the mortality rate associated with intestinal IR remains at 50–80% [2]. The intestinal mucosa is most vulnerable to IR in a classic cascade damage mode, in which intestinal epithelia are initially injured and then inflammation driven by immune cells is triggered, in turn further destroying the epithelia [3]. Therefore, attempts to find drug targets to mitigate epithelial damages can be regarded as fighting the fire from the source. Previous studies on therapeutic molecular targets for intestinal IR injury have mainly relied on hypoxic 2D primary epithelial cells or cell lines using a tri-gas incubator filled with 1% oxygen or animal IR models [4].

These 2D cell models do not capture the spatially heterogeneous organization of native epithelial phenotypes. Furthermore, the oxygen

Peer review under responsibility of KeAi Communications Co., Ltd.
* Corresponding author. Research Institute of General Surgery, Jinling Hospital, School of Medicine, Southeast University, Nanjing, 210009, China.
** Corresponding author.
*** Corresponding author. Research Institute of General Surgery, Jinling Hospital, School of Medicine, Southeast University, Nanjing, 210009, China.
E-mail addresses: panyc@njtech.edu.cn (Y. Pan), wuxiuwen@nju.edu.cn (X. Wu), Jiananr@nju.edu.cn (J. Ren).

https://doi.org/10.1016/j.bioactmat.2023.07.001
Received 7 April 2023; Received in revised form 11 June 2023; Accepted 1 July 2023
2452-199X/© 2023 The Authors. Publishing services by Elsevier B.V. on behalf of KeAi Communications Co. Ltd. This is an open access article under the CC BY-NC-ND license (http://creativecommons.org/licenses/by-nc-nd/4.0/).

decline requires up to 24 h [5], which is different from the *in vivo* IR process where the tissue hypoxia is ultrafast and epithelia start to disintegrate after around 45 min of ischemia [6]. The long-term duration of oxygen decline is likely to conceal the therapeutic targets by reshaping the expression maps of genes and proteins as mammals have an intrinsic adaptive competence to hypoxia [7–10]. Moreover, in animal IR models, intestinal epithelia are easily affected by adjacent immune cells, thus possibly impeding the discovery of initiating molecular targets. Owing to the lack of precise models integrating epithelial similarities and comparable oxygen dynamics, drug development to rescue intestinal IR injury faces obstacles.

Based on the discovery of lgr5^{+} intestinal stem cells (ISCs) and growth factor-inducing strategy, intestinal organoids have been developed in the form of a 3D cell cluster acquiring all the types of intestinal epithelial cells [11]. The intestinal organoids can maintain the genetic signature of the donor's intestine and offer a platform for the investigation of disease mechanisms and drug screening [12,13], but they fail to depict intestinal morphological features, natural biochemical gradients, and biophysical stimulations. Interestingly, intestinal organoid-on-a-chip is emerging to increase the controllability of organoids, such as the application of diverse stimuli (e.g., fluid flow, mechanical deformation, and hormones) to regulate intestinal morphogenesis and even the direct rearrangement of epithelia to be tube-shaped and self-renewal [14,15]. However, the current organoid-on-a-chip approaches rarely achieve multisystem interactions that play vital roles in intestinal diseases [16]. Given the importance of learning mechanisms and developing drugs for intestinal IR injury, to implement blood vessel-originated hypoxia and reoxygenation (HR) in intestinal organoid-on-a-chip is of great urgency and significance [17].

Inspired from the natural structure of intestinal villi in which the central capillary is wrapped with circling intestinal epithelia and nourishes them, we reported a biomimetic intestinal organoid-on-a-chip embedded with artificial microvessels. The artificial microvessels with the hollow structure were manufactured using homemade co-axial microfluidic equipment based on pH-responsive ZIF-8/sodium alginate (SA). Followed by Matrigel coating, human umbilical vein endothelial cells (HUVECs) were able to adhere to the inner wall and respond to hypoxic environment by the activation of inflammatory reactions. Then,

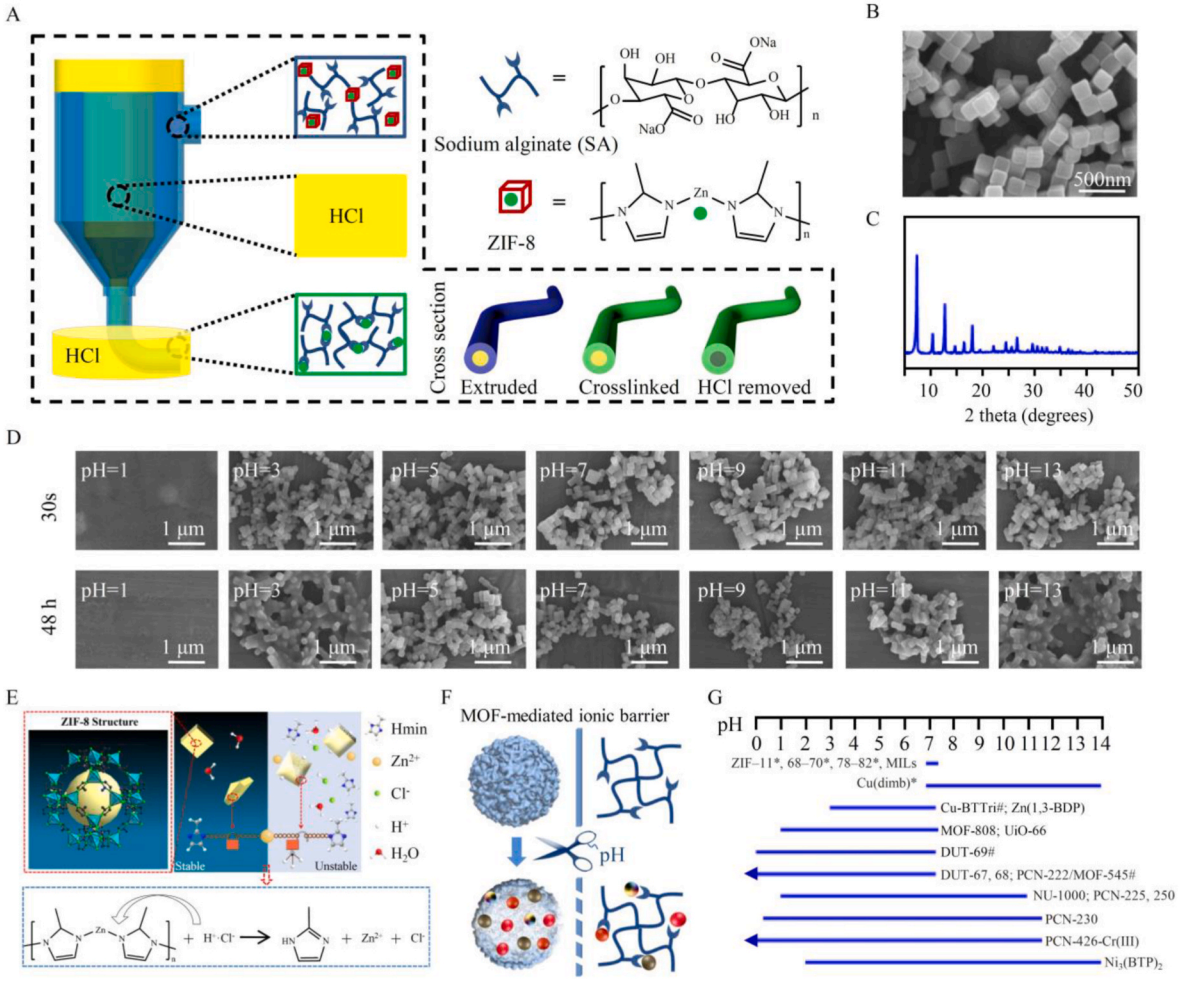

Fig. 1. Fabrication of vessel scaffolds based on the mechanism of pH-sensitive MOF/anionic polymer crosslinking. (A) The scheme of vascular structure-like hollow fiber production based on pH-responsive ZIF-8/SA crosslinking. (B) The production of uniform and cubic ZIF-8 nanoparticles imaged by SEM. (C) XRD characterizes the high crystallinity of ZIF-8 nanoparticles. (D) The SEM images of ZIF-8 nanoparticles were observed after 30-min or two-day treatment of a different pH. (E) The mechanism by which low pH-induced protonation of the ligand, 2-methylimidazole (Hmin), unlocks the coordination bonds can account for the instability of ZIF-8 nanoparticles. (F) The proposal of "MOF-mediated ionic barrier" for the solidification of polymer networks with an accessible pH adjustment. (G) The summary of many other MOF families that can achieve the function of "MOF-mediated ionic barrier". The line indicates the pH range that MOFs can tolerate. An arrow indicates that the MOF can withstand a pH of less than 0. "*" and "#" mean that the stability in aqueous acid or aqueous base has not been reported, respectively. ZIF, zeolitic imidazolate framework; dimb, 1,4-bis(1*H*-imidazole-4-yl)benzene; BTTri, 1,3,5-tris(1*H*-1,2,3-triazol-5-yl); 1,3-BDP, 1,3-benzenedipyrozolate; UIO, University of Oslo; DUT, Dresden University of Technology; PCN, porous coordination network; NU, Northwestern University; BTP, 1,3,5-tris(1*H*-pyrazol-4-yl)benzene.

the microvessels and intestinal organoids were assembled to a chip in an arrangement of vessels surrounded by organoids.

Through finite element analysis and oxygen meter detection, the oxygen microenvironment of intestinal organoid-on-a-chip was found to be continuously and sharply decreased. It reached an absolute hypoxic state within a much shorter time (3 h) compared with the tri-gas incubator (24 h). When the neighboring artificial microvessels were damaged, or there was an insufficient oxygen supply, the intestinal organoid-on-a-chip was bio-responsive in terms of cell oxidative stress and apoptosis. Such hypoxic organoids were analyzed by RNA-sequencing to screen key therapeutic targets by setting the normoxic samples as control. *Olfm4* was revealed as the most significantly down-expressed gene, and was verified to be a therapeutic target for intestinal IR injury. Of note, the protective role of OLFM4 in the intestinal epithelia in IR injury is acknowledged for the first time, which undoubtedly shows the importance of recapitulating the oxygen dynamics for the microfluidic organoid-on-a-chip to screen drug targets accurately.

2. Results

2.1. Vascular structure-simulated hollow fibers based on pH-sensitive ZIF-8/SA crosslinking

Extrusion-based co-axial microfluidic technology was applied to produce blood vessel-like hollow fibers. As shown in Fig. 1A, the outer nozzle was filled with a 3 wt% SA solution dispersed homogeneously with 4 mg/mL ZIF-8 nanoparticles, a kind of zinc (Zn)-based metal-organic frameworks (MOFs). We assumed that, based on the pH sensitivity of MOFs, ZIF-8 nanoparticles could be lysed, and Zn^{2+} was released to crosslink with SA. Such a pre-dissolved ZIF-8/SA solution theoretically enabled a spatially evenly distributed crosslinking of zinc ions with SA, and the resulted network structure could mimic extracellular matrix (ECM) of blood vessel wall.

To confirm the assumption, we first synthesized cube-shaped ZIF-8 nanoparticles at the size of ~120 nm (Fig. 1B). The x-ray diffraction (XRD) characterization indicated a high crystallinity of the ZIF-8 structure (Fig. 1C), and the energy dispersive spectrometer (EDS) analysis showed the weight percentage of the Zn element to be 28.69% (Fig. S1). Then, the stability of ZIF-8 was investigated. Through a pH gradient processing, it was observed with scanning electron microscopy (SEM) that a pH of 1 contributed to a complete acidolysis of ZIF-8 structure within the least operating time of ~30 s, while a pH over 3 did not cause apparent morphological changes in 48 h (Fig. 1D, Fig. S2A). More accurately, by recording turbidity, such acidolysis occurred instantly at pH = 1, accompanied by the robust release of Zn^{2+} in the supernatant (Video S1, Fig. S2B). This phenomenon is attributed to the protonation of the ligands (2-methylimidazole), thus rupturing the coordination bonds (Fig. 1E).

Consistently, after adjusting the ZIF-8/SA solution to be pH = 1, the disappearance of the peak at 12.6° in XRD detection and the stretching peaks at 1,309.4 cm^{-1}, 995.1 cm^{-1}, 759.8 cm^{-1}, and 694.7 cm^{-1} in FTIR spectra also suggested the destruction of the ZIF-8 crystal structure (Figs. S3A and B). Meanwhile, the asymmetric and symmetric stretching vibration of carboxyl groups at 1,589 cm^{-1} and 1,409.7 cm^{-1} were decreased compared with SA, and the band at 1,727.9 cm^{-1} assigned to C=O stretching emerged (Fig. S3B), which were both attributed to the crosslinking of Zn^{2+} with the carboxyl groups of SA [18]. Furthermore, the acquired scaffold showed a very quick gelation time at pH = 1 by exhibiting an immediate crossing point of storage modulus (G′) and loss modulus (G") (Fig. S3C) and presented a typical porous structure (Fig. S3D). In contrast, the stability of ZIF-8 was excellent at pH = 7, and the release of Zn^{2+} was extremely low, so that one-year accumulation of Zn^{2+} still could not trigger the crosslinking of SA, as revealed by a vial tilting method (Fig. S4). Therefore, the concept of a MOF-mediated ionic barrier is proposed here (Fig. 1F), which can be used to solidify polymer networks by regulating the pH value. Moreover, apart from ZIF-8, this approach can be generalized among many other MOF families according to their pH stabilities (Fig. 1G) [19].

We then investigated the optimal concentration of ZIF-8 and SA to optimize mechanical strength. Compressive tests (Figs. S5A and B) indicate that increasing ZIF-8 and SA concentration could improve toughness. Given the saving of materials and acquisition of toughness, 4 mg/mL ZIF-8 and 3 wt% SA (mass ratio = 4: 30) were chosen for later experiments. In this formula, G′ and G" of the scaffold were ~1,000 Pa and ~100 Pa, respectively (Fig. S5C), and the precursor solution could be processed with nozzle extrusion owing to the shear-thinning property (Fig. S5D) [20].

On this basis, we designed a piece of homemade co-axial microfluidic equipment to produce blood vessel-like hollow fibers (Figs. S6A and B). Through adjusting nozzle size and flow rate (Fig. S6C), the extruded hollow fibers exhibited the tunability of lumen diameters and wall thickness (Fig. 2A, Figs. S6D and E). Moreover, the intraluminal liquid was removable and reperfusable (Fig. 2B, Video S2), thus allowing surface modification and cell carrier. Such hollow fibers could be manufactured continuously and homogeneously (Video S3, Fig. S6F) and rearranged in circles with structural stability after freeze-drying (Fig. 2C). Owing to the flexibility, complex shapes such as butterfly, apple, and the grid could be woven up using hollow fibers (Fig. 2D).

2.2. Fabrication of living artificial microvessels by loading HUVECs

The native microvessels have the characteristics of permeability, elasticity, and blood pressure tolerance; therefore, these aspects ought to be evaluated on the microvessel-like hollow fibers. We injected a dye solution, acid blue, into the lumen and sealed the fiber by tying a knot on two ends (Fig. 3A). The dye permeated the hollow fiber wall and reached the concentration balance in 60 min (Fig. 3B). Furthermore, the permeation speed of dyes with different molecule weights was compared. Initially, a low-weight molecule, FITC, diffused faster than a high-weight molecule, BSA-FITC, and eventually, the two dyes penetrated the wall completely (Fig. 3C and D). In addition, the increased wall thickness of hollow fibers was found to retard the release of dyes (Fig. 3E). As for the elasticity, stretching tests were performed in the hollow fibers, which showed the competence to elongate ~80% of its length and bear 200 times its own weight (Fig. 3F and G). Moreover, the hollow fibers could tolerate a bursting pressure ranging from ~80 KPa to ~130 KPa, which significantly exceeded the mean artery pressure (MAP) (~11 KPa) (Fig. 3H).

Next, we constructed bio-interfaces for hollow fibers using Matrigel, an extracellular matrix (ECM) analog containing Arg-Gly-Asp (RGD) sequences capable of binding with integrin receptors for cell adhesion and spread. It was confirmed in Fig. S7 that the Zn^{2+}/SA scaffold coated with a layer of 20 v/v% Matrigel facilitated the adhesion and spread of HUVECs. In contrast, the scaffold alone led to an abnormal spherical shape. Based on this outcome, we decorated the inner surface of hollow fibers with Matrigel, which was then transfused with HUVECs. In the beginning, the cells were circular-shaped, but they started to adhere to the inner surface and spread out with time going (Fig. 4A). On day 3, the cells presented a high survival ratio, maintained the expression of the specific marker of vascular endothelial cells (CD 31), and showed a spreading morphology of cytoskeleton by F-actin staining (Fig. 4B). Moreover, the CCK-8 assay demonstrated proliferative capacity (Fig. 4C). These findings suggest that the Matrigel-coated hollow fiber can create a HUVEC-friendly environment.

The bio-responsiveness is a dominant feature of qualified artificial microvessels (Fig. 4D); therefore, we further investigated it under an HR environment created by a tri-gas incubator. After 24 h of hypoxia, hypoxia-inducible factor-1α (HIF-1α) was highly expressed compared with that of the HUVECs cultured in normoxia. Treated with additional 1-h reoxygenation, the cells showed a significant increase in the phosphorylation of p65 (Fig. 4E), suggesting that HR could trigger the

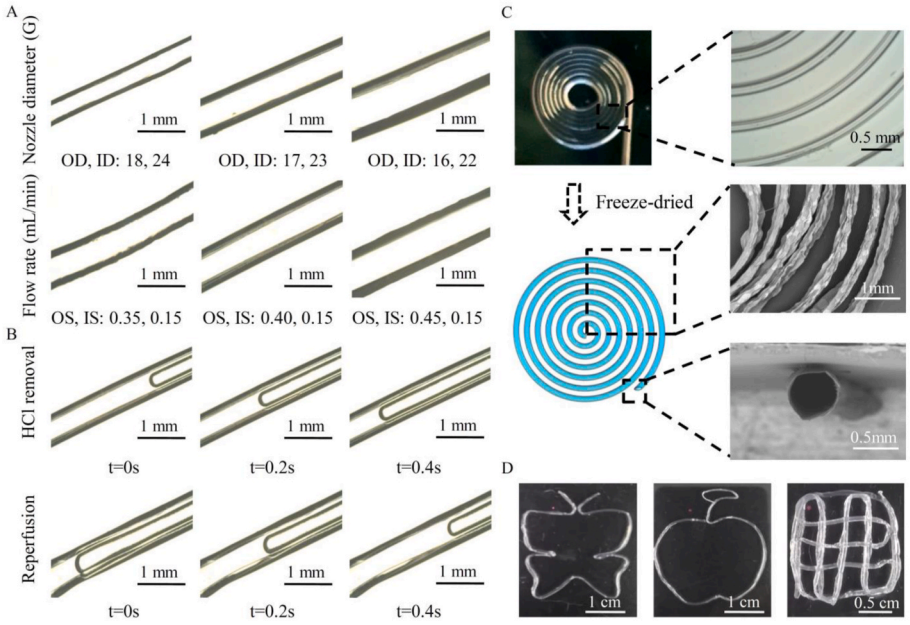

Fig. 2. Hollow structure of the vascular scaffold constructed by co-axial microfluidic extrusion. (A) The regulation of hollow fiber's lumen diameter and wall thickness by nozzle diameter and flow rate of microfluidic equipment. OD, outer diameter; ID, internal diameter. The unit is G. OS, outer speed; IS, internal speed. The unit is mL/min. (B) The reperfusability of intraluminal liquid can enable to construct desired bio-interfaces on the internal surface of hollow fibers. (C) The structural flexibility and fidelity of hollow fibers after coiling and freeze-drying. (D) The hollow fibers weave up complex shapes such as butterflies, apples, and grids.

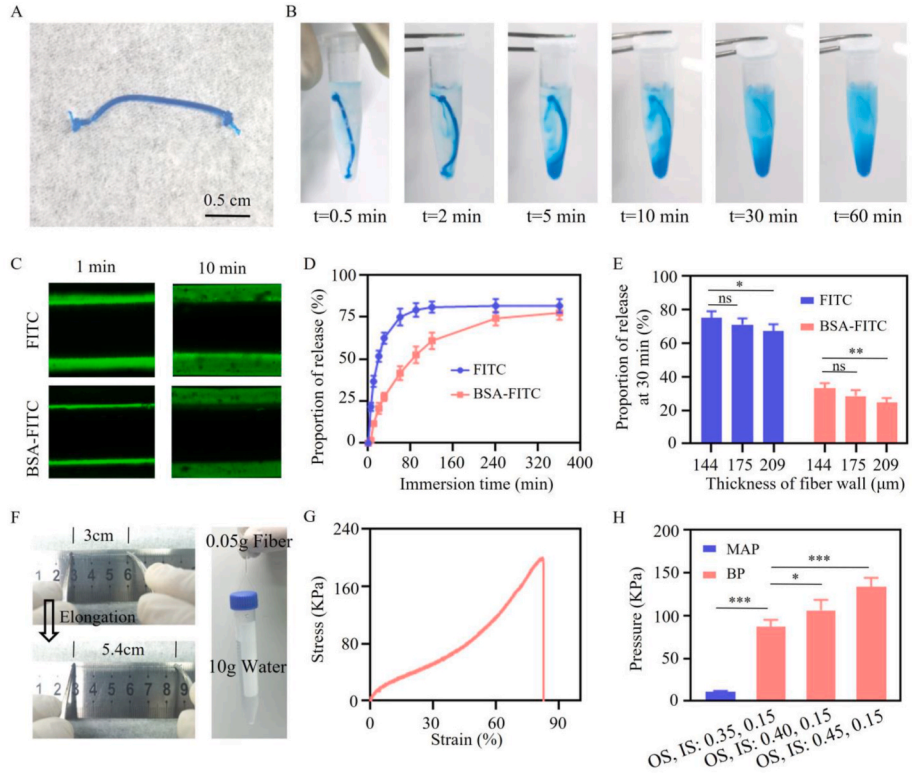

Fig. 3. Similarities of the hollow fibers with natural vessels in terms of physical properties. (A) The sealed hollow fiber is filled with an acid blue aqueous solution to test permeability. (B) The permeating process of acid blue across the wall of the hollow fiber (C) Comparison of permeating speed of dyes (e.g., FITC and BSA-FITC). with different molecular weights. FITC, fluorescein isothiocyanate; BSA, bovine serum albumin. (D) Quantitative analysis of permeating dynamics of dyes (e.g., FITC and BSA-FITC) with different molecule weights, n = 4. (E) The regulation of dyes' permeating speed by the wall thickness of the hollow fiber, n = 4. (F) The representative images demonstrate that the hollow fiber can be elongated or bear 200 times its own weight. (G) The tensile stress-strain of the hollow fiber. (H) The BP of hollow fibers with different wall thickness compared with MAP, n = 4. BP, bursting pressure; MAP, mean artery pressure. *p < 0.05; **p < 0.01; ***p < 0.001; ns, not significant.

activation of NF-Kappa B signaling in the artificial microvessels. Moreover, it was found by cell staining with oxygen-free radical probe and TNF-α antibody that the production of reactive oxygen species (ROS) and pro-inflammatory TNF-α cytokines was increased (Fig. 4F and G). In contrast, in the cell lysate, superoxide dismutase (SOD) with ROS clearance was decreased after HR. Simultaneously, the malondialdehyde (MDA), an oxidative product, and pro-inflammatory cytokines, IL-1β and TNF-α, were accumulated (Fig. 4H and I). These data all confirmed the responsiveness of artificial microvessels to HR through oxidative stress and inflammatory reactions.

2.3. Microfluidic intestinal organoid-on-a-chip for fast oxygen dynamics

Before constructing a biomimetic chip, we first described pathophysiological alterations in mice following intestinal ischemia (30 min) and reperfusion. It was found that intestinal IR injury could result in the death of mice and intestinal mucosa damage in terms of epithelial cell detachment, oxidative stress, and cell apoptosis (Fig. S8). With more molecular insights, the apoptosis signals by TdT-mediated dUTP nick end labeling (TUNEL) staining were present in the apical part of intestinal villi, and tight intercellular junctions stained with occludin were

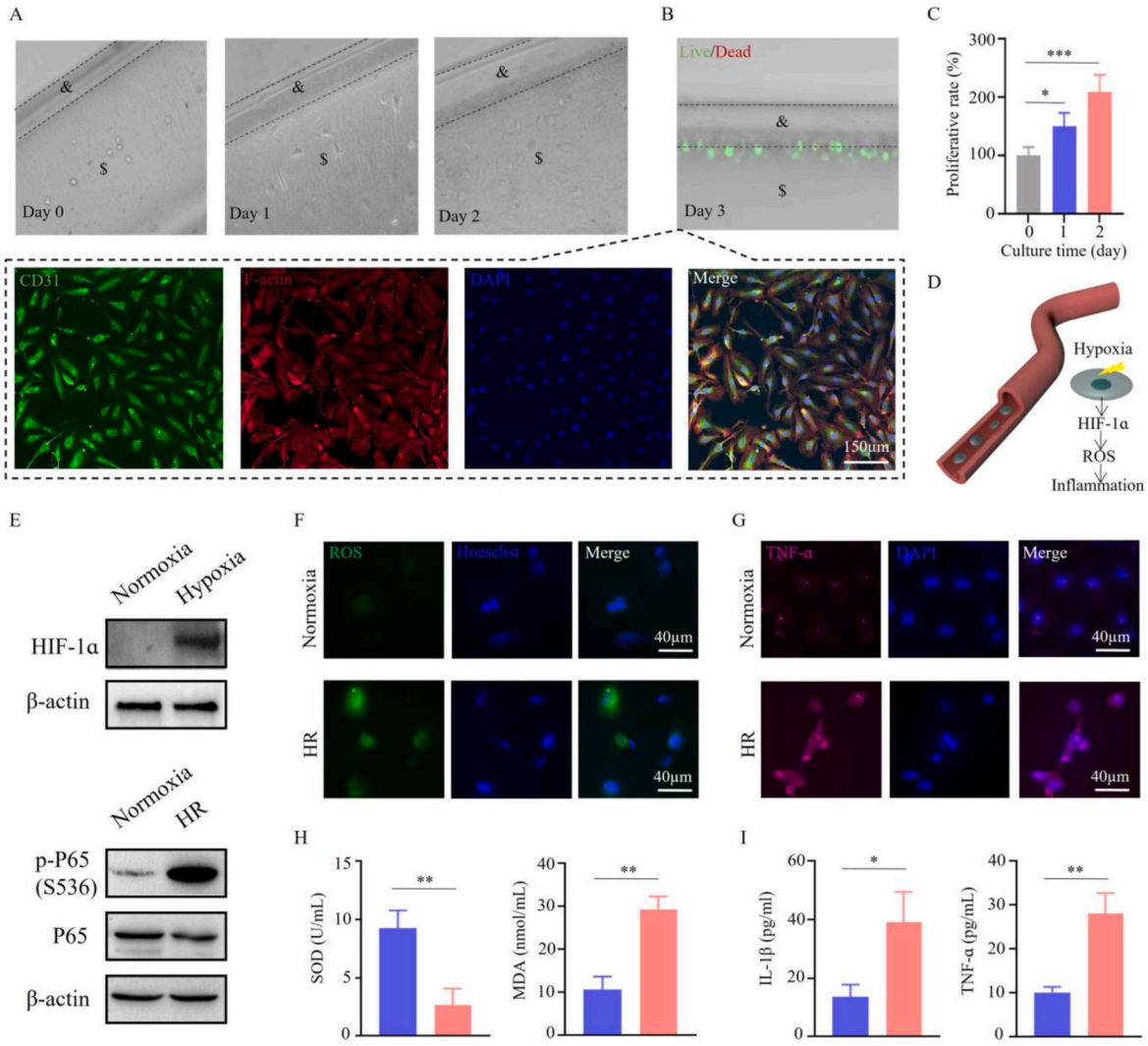

Fig. 4. Fabrication and bio-responsiveness of artificial vessels. (A) The adhesion and proliferation of HUEVCs laden in the Matrigel-coated hollow fiber. &, the wall of artificial vessels; $, the lumen of artificial vessels. (B) The live/dead staining, biomarker staining (CD31), and cytoskeleton staining (F-actin) of HUEVCs adhering to the wall of artificial vessels at day 3. &, the wall of artificial vessels; $, the lumen of artificial vessels. (C) The proliferation rate of HUVECs in the hollow fiber, n = 4. (D) The schematic diagram of bio-responsive mechanism to cell hypoxia. (E) HUVEC-laden hollow fiber can sense hypoxia by increasing HIF-1α and response to HR by conducting the phosphorylation of p65 to activate NF-Kappa B signaling. (F) Representative images of ROS production in HUVECs of artificial vessels treated with normoxia or HR. (G) Representative images of TNF-α expression in HUVECs of artificial vessels treated with normoxia or HR. (H) Quantitative analysis of SOD and MDA in the cell lysate of HUVECs of artificial vessels treated with normoxia or HR, n = 3. (I) Quantitative analysis of IL-1β and TNF-α in the cell lysate of HUVECs of artificial vessels treated with normoxia or HR, n = 3. *$p < 0.05$; **$p < 0.01$; ***$p < 0.001$.

undermined due to IR injury (Fig. 5A). Additionally, capillaries labeled with CD31 showed evident pro-inflammatory signals of TNF-α (Fig. 5B). These clues implied that both vascular and intestinal systems participate in IR injury at the very early stage.

Then, we rebuilt the blood vessel-nourished intestinal system *in vitro* by acquiring intestinal stem cell-derived organoids (Fig. S9) and fabricating a chip embedded with intestinal organoids and embedded with artificial miacrovessels (Fig. 5C). This chip consisted of a polydimethylsiloxane (PDMS) bottom and a PDMS cover casted from a polymethyl methacrylate (PMMA) model produced by a computer numerical control (CNC) router (Figs. S10A and B). First, HUVECs-laden hollow fibers used as artificial vessels were placed in the channel of the PDMS chip, and then the semi-cylindrical voids besides the hollow fibers were injected with a Matrigel precursor solution mixed with mature intestinal organoids and ROS probe. Afterward, a microfluidic pump was connected with artificial microvessels to perfuse different pretreated culture media (Fig. S10C).

After perfusing culture medium with hydrogen peroxide or low-concentration oxygen (~25 μmol/L), the signal of ROS production was significantly increased compared to the normoxic culture medium (~180 μmol/L) (Fig. 5D). Moreover, reoxygenation following hypoxia by the subsequent treatment with normoxic culture medium would exacerbate oxidative stress damage on intestinal organoids, implying that this chip could mimic intestinal IR injury. To finely describe the HR process sensed by intestinal organoids, simulation of oxygen diffusion was conducted with COMSOL software according to the experimental conditions presented in Tables S1 and S2. The result indicated that it took around 3 h to reach a steady hypoxia state and 1 h to restore 70% of the normal oxygen concentration (Fig. 5E and F; Video S4 and S5). At the beginning of the hypoxia stage and the reoxygenation stage, oxygen concentration of intestinal organoid-laden Matrigel changed very quickly, just as the sharp change of oxygen after vascular embolization *in vivo*. The oxygen concentration values measured by an oxygen meter were consistent with the simulated situation. Notably, an HR cycle using the microfluidic chip consumed a much shorter time (4 h) in total than using a tri-gas incubator (25 h) (Fig. 5G). This was because the gas

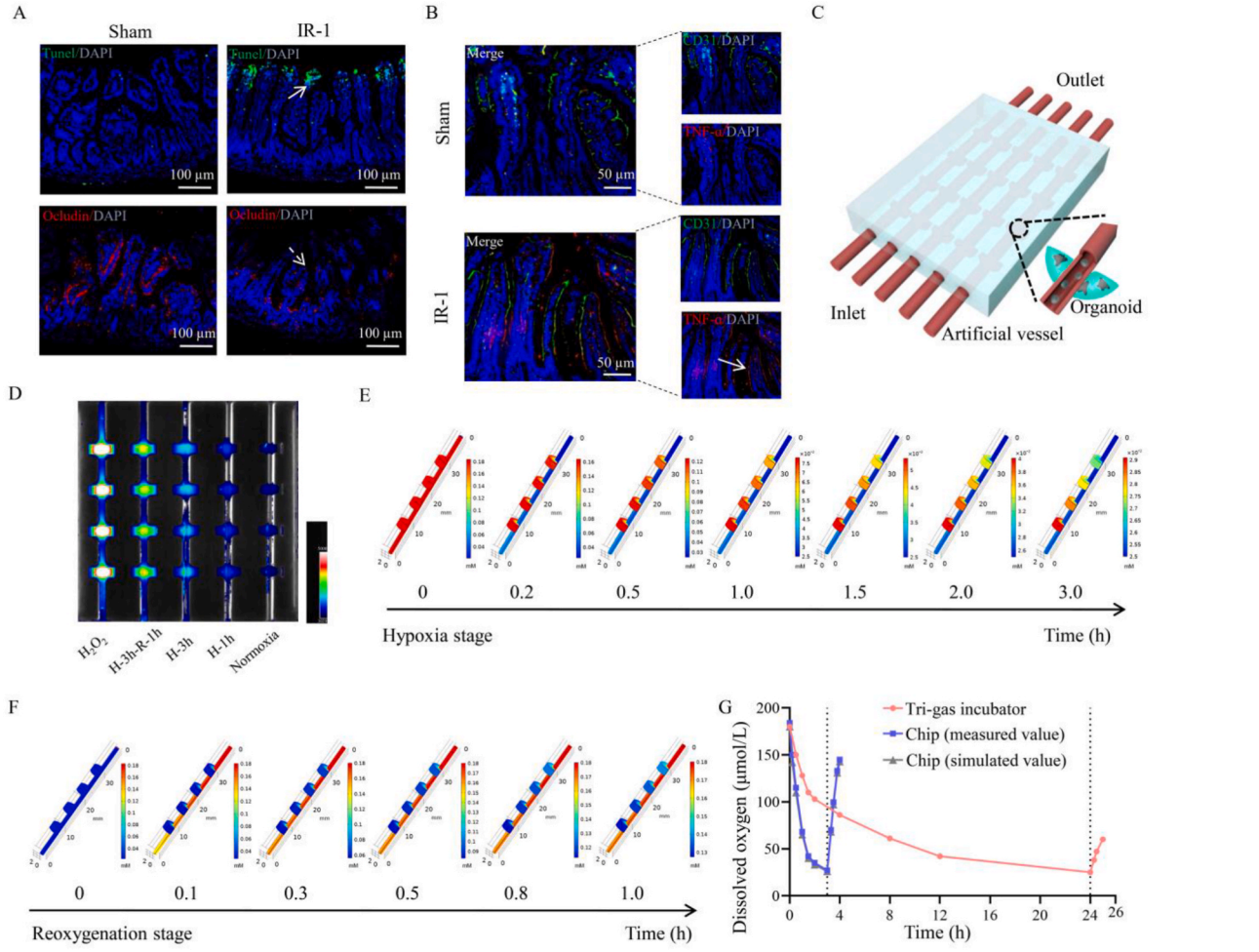

Fig. 5. Fabrication of artificial vessel-embedded intestinal organoid-on-a-chip with the ultrafast HR ability and biomimetic structure. (A) The small intestine is damaged following intestinal IR injury and presents the intestinal epithelial apoptosis (labeled with solid arrow) and the interruption of tight connects (labeled with dashed arrow). (B) Pro-inflammatory reaction (labeled with solid arrow) is significantly aggravated in intestinal epithelial capillaries labeled with CD 31 following intestinal IR injury. (C) The schematic diagram of a microfluidic intestinal organoid-on-a-chip embedded with artificial microvessels, which can simulate the native structure of intestinal epithelia nourished by central capillaries. (D) ROS production of the intestinal organoid-on-a-chip with different treatments. H, hypoxia; R, reoxygenation. (E) The COMSOL simulation of hypoxia process for the intestinal organoid-on-a-chip. (F) The COMSOL simulation of reoxygenation process for the intestinal organoid-on-a-chip. (G) The comparison of dissolved oxygen during HR between the chip model and tri-gas incubator.

diffusion in our chip system occurred in a liquid-to-liquid interface instead of a gas-to-liquid interface, which is much closer to the way of *in vivo* oxygen transportation.

2.4. *Bio-responsiveness and genetic signatures of intestinal organoid-on-a-chip*

We then identified the bio-responsiveness of intestinal organoids in the case of abnormalities in the blood vessel supply. First, the wall of the artificial vessel was damaged by ultraviolet (UV) exposure (Fig. 6A, Fig. S11). This pre-injured vessel sparked ROS production (Fig. 6B) and caused apoptosis signaling activation for intestinal organoids (Fig. 6C). In addition, "blood flow"-induced HR was also verified to promote ROS generation and intestinal organoid apoptosis directly, accomplished by the increase of lactate dehydrogenase (LDH) and caspase-3 activities (Fig. 6D, E, F). These data suggested that intestinal organoids were bio-responsive to various pathological stimuli of neighboring vessels in a similar form of intestinal damages during IR injury.

We performed RNA-sequencing on the harvested intestinal organoids from the chip treated with normoxia or HR to identify differentially expressed genes and then explore potential molecular mechanisms underlying HR-induced injury. The clustering analysis revealed that the samples showed a consistent hierarchical clustering for the biological replicates and an evident separation by HR treatment based on the 1301 genes with differential expressions (Fig. 6G). Among these genes, 741 genes were significantly up-regulated and 560 genes were down-regulated in the organoids treated with normoxia *vs* HR. Furthermore, through the KEGG enrichment analysis, we found that adenosine triphosphate (ATP)-dependent metabolic or synthetic processes of vital molecules were significantly influenced by HR such as DNA, carbohydrates, and amino acids (Fig. 6H), because the ATP generated from the mitochondrial respiratory chain was inhibited due to the insufficient oxygen supply [21]. Moreover, the function of cytochrome P450, a heme-thiolate protein involved in oxidative degradation of various compounds, was impaired, thereby causing inevitable cellular oxidative stress [22]. Additionally, the volcano plot labeling differentially expressed genes revealed prominent transcriptional alterations in inflammatory regulations (e.g., *Olfm4*, *Card11*, *Egr1*, *Serinc3*, *Aldoc*, *Ddit4*, *Impdh2*, and *Ndrg1*), and molecular transportation and metabolism (e.g., *Selenbp1*, *Gbe1*, *Syde2*, and *Pgm2*) (Fig. 6I). Among them, *Olfm4* was the gene most significantly expressed at low levels, which we guessed was possibly responsible for the damage of intestinal organoids induced by HR. Real-time quantitative PCR was used to verify the findings of RNA-sequencing. Specifically, transcription of *Olfm4* was reduced after

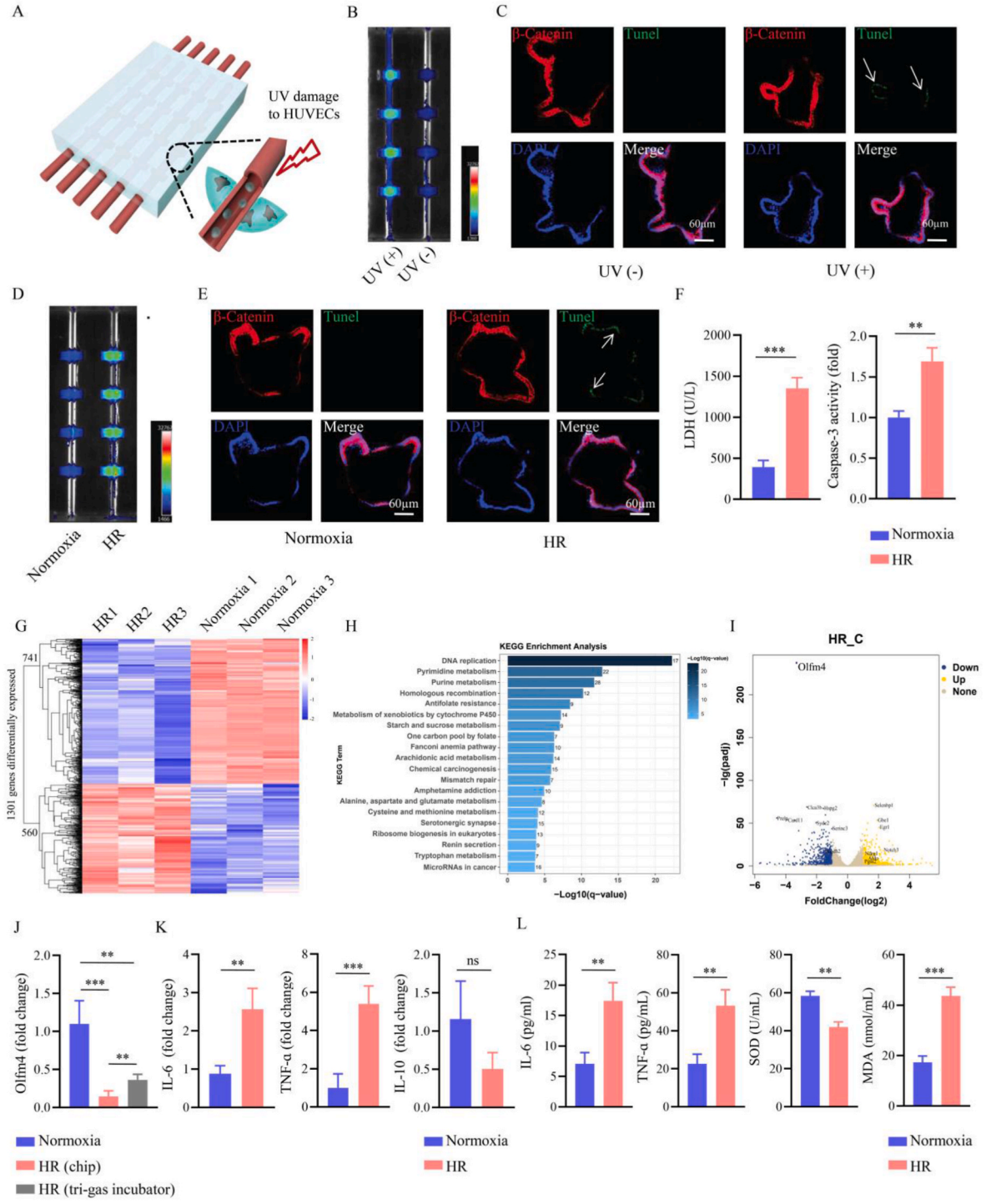

Fig. 6. Bio-responsiveness and genetic signatures of microfluidic intestinal organoid-on-a-chip. (A) The schematic diagram of intestinal organoid damage caused by UV-induced artificial vessel injury. (B) The elevated ROS production of intestinal organoids resulted from UV-triggered artificial vessel injury. (C) The increase of cell apoptosis in intestinal organoids resulted from UV-triggered artificial vessel injury. The arrows label the apoptotic cells. (D) The increase of ROS production in HR-treated intestinal organoids. (E) The increase of cell apoptosis in HR-treated intestinal organoids. The arrows label the apoptotic cells. (F) Comparison of LDH release and caspase-3 activity in intestinal organoids treated with normoxia or HR, n = 4. (G) The heatmap of 1301 genes differentially expressed in intestinal organoids treated with normoxia *vs* HR (up-regulated: 741; down-regulated: 560). (H) The KEGG analysis of differentially-enriched pathways in HR-treated intestinal organoids compared to those treated with normoxia. (I) The volcano plot labeling differentially expressed genes, among which *Olfm4* is the most significantly gene expressed at low levels. (J) Real-time quantitative PCR of the gene of interest, *Olfm4*, to verify the findings of RNA-sequencing and compare the expression levels between two HR patterns by using the chip or the tri-gas incubator, n = 4. (K) Comparison of transcriptional levels of inflammatory cytokines (e.g., *IL-6*, *TNF-α*, and *IL-10*) in the intestinal organoids treated with HR or normoxia using the chip, n = 4. (L) Quantitative analysis of IL-6, TNF-α, SOD, MDA in the intestinal organoids on chip treated with HR or normoxia, n = 3. **p < 0.01; ***p < 0.001; ns, not significant.

HR compared with normoxia in the chip. More interestingly, due to the different HR dynamics, *Olfm4* of the organoids in the chip (3 h of hypoxia and 1 h of reoxygenation) was much lower-expressed than that of the organoids in the tri-gas incubator (24 h of hypoxia and 1 h of reoxygenation) (Fig. 6J). It implied that the discovery of *Olfm4* was oxygen dynamics-dependent, and our chip achieving faster HR could present a more significant transcriptional difference for *Olfm4*. This finding highlights the importance on the recapitulation of an appropriate oxygen dynamics for *in vitro* models to simulate oxygen-related diseases.

Moreover, the transcriptional level and protein expression of classic pro-inflammatory cytokines (e.g., IL-6 and TNF-α) were increased in the intestinal organoid-on-a-chip after HR (Fig. 6K and L). The levels of ROS scavenger, superoxide dismutase (SOD), were decreased in HR-treated intestinal organoids on chip, and the oxidation product, malondialdehyde (MDA), was accumulated. These altogether suggested that the intestinal organoids in the chip could present an inflammatory state with cellular oxidative stress when treated with fast HR.

2.5. Biological functions of OLFM4 on intestinal IR injury

To investigate the relation of OLFM4 with the inflammatory response of intestinal organoid-on-a-chip after HR, we constructed a specific lentivirus encoding the gene of green fluorescent protein (GFP) and *Olfm4* shRNA or *Olfm4* transcript to inhibit or enhance the *Olfm4* expression, respectively (Fig. S12). After a series of lentivirus transduction procedures (Fig. 7A), the intestinal organoids that were successfully infected became GFP+ (Fig. 7B and C). Then, the transinfected intestinal organoids were embedded in the chip following the treatment with 3-h hypoxia and 1-h reoxygenation. As a result, interference of *Olfm4* expression increased the transcription of pro-inflammatory cytokines, such as *TNF-α*, *IL-6*, and *IL-1β*. In contrast, *Olfm4* overexpression suppressed them, which preliminarily revealed its protective functions on HR-sparked inflammation. To double verify the findings, we further treated these transfected intestinal organoids off chip using the classic tri-gas incubator with 24-h hypoxia and 1-h reoxygenation. The effects off chip were almost the same as the effects on chip (Fig. 7D), which confirmed the beneficial role of *Olfm4* expression on reducing inflammation.

Moreover, to address the potential therapeutic values, OLFM4 recombinant protein was loaded by liposome for intracellular delivery in FHC (Fig. 7E). The liposome was prepared via thin-film hydration at the size of 100–200 nm that could greatly improve the intracellular uptake efficiency of protein (e.g., BSA-FITC) after a 6-h co-culture (Fig. S13). BSA-FITC without liposome carriers hardly entered the cells. Similarly, OLFM4 alone was absent in FHC but present when carried by liposome (Fig. 7F). Since OLFM4 was reported to bind the nucleotide oligomerization domain-1 (NOD1) and −2 (NOD2) that negatively regulated the NF-kappa B pathway during *H. pylori* infections [23], we further examined whether OLFM4 protected HR injury via the inhibition of NF-kappa B signaling. The experimental results confirmed our assumption that OLFM4 in the cytoplasm of FHC would impede the phosphorylation of p65 and inactivate the NF-kappa B pathway. Moreover, the transcriptional levels of pro-inflammatory cytokines were lowered by

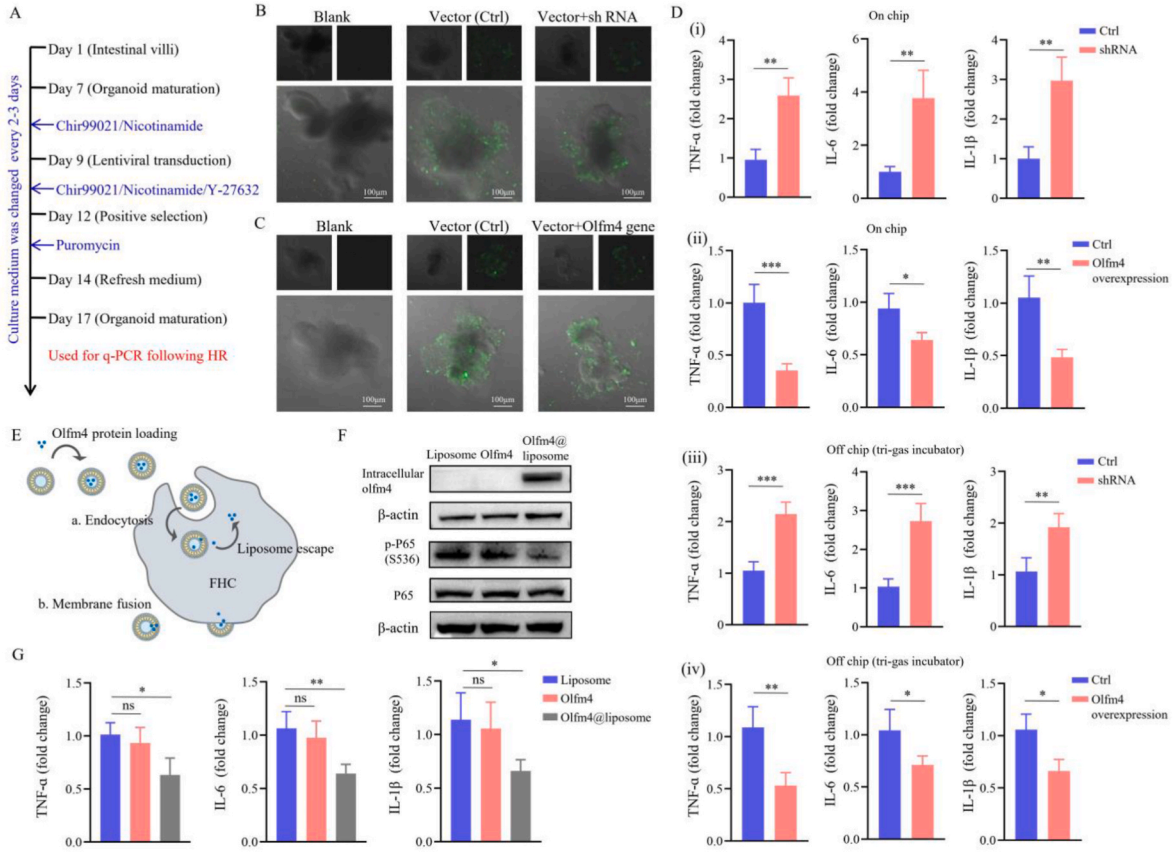

Fig. 7. Regulation of OLFM4 on HR-induced intestinal inflammation *in vitro*. (A) The protocol for the lentivirus transduction of intestinal organoids. (B, C) Success on lentivirus infections on intestinal organoids confirmed by the emerging of GFP. (D) Transcriptional differences of pro-inflammatory cytokines in the HR-treated intestinal organoids with *Olfm4* interference or *Olfm4* overexpression compared with those infected with vector lentivirus. i and ii: on chip HR treatment; iii and iv: off chip HR treatment based on tri-gas incubator. n = 4. (E) The schematic diagram of intracellular delivery of OLFM4-loaded liposome. (H) The verification of intracellular delivery of OLFM4 by liposome and its inhibitory effects on the p65 phosphorylation of NF-kappa B signaling. (G) Quantitative analysis of genes coding pro-inflammatory cytokines in HR-treated FHC with different pre-interventions using blank liposome, OLFM4, or OLFM4-loaded liposome, n = 3. *p < 0.05; **p < 0.01; ***p < 0.001; ns, not significant.

the increase of intracellular OLFM4 (Fig. 7G).

Next, we explored OLFM4 dynamic changes during intestinal IR injury. With the reperfusion time going, the intestinal damage and pathological scoring were increased (Figs. S14A and B). The transcription (e.g., *IL-1β*) and secretion (e.g., TNF-α) of pro-inflammatory cytokines were also gradually elevated, but the transcription and expression of *Olfm4* were first raised and then declined (Fig. 8A and B; Figs. S14C and D). Moreover, fluorescence in situ hybridization of *Olfm4* RNA showed a consistent trend of initial increase followed by a decrease (Fig. 8C). OLFM4, which was located at intestinal crypts, could be used as a marker of ISCs [24]. In addition, an incisional hernia patient sample with spatially different damage extents revealed that moderate ischemia caused the increase of *Olfm4* expression compared with the mild lesion. In contrast, severe ischemia led to down-expression of *Olfm4* (Fig. 8D). Based on these findings, we hypothesized that ISCs could temporarily resist the intestinal IR injury by adaptive OLFM4 production, but it failed to prevent IR injury because of OLFM4 exhaustion.

To verify this hypothesis, we conducted intraperitoneal injection of lentivirus at 1×10^9 copies/week for three weeks to gain the expression of *Olfm4* in intestinal tissues. We investigated the effects on intestinal

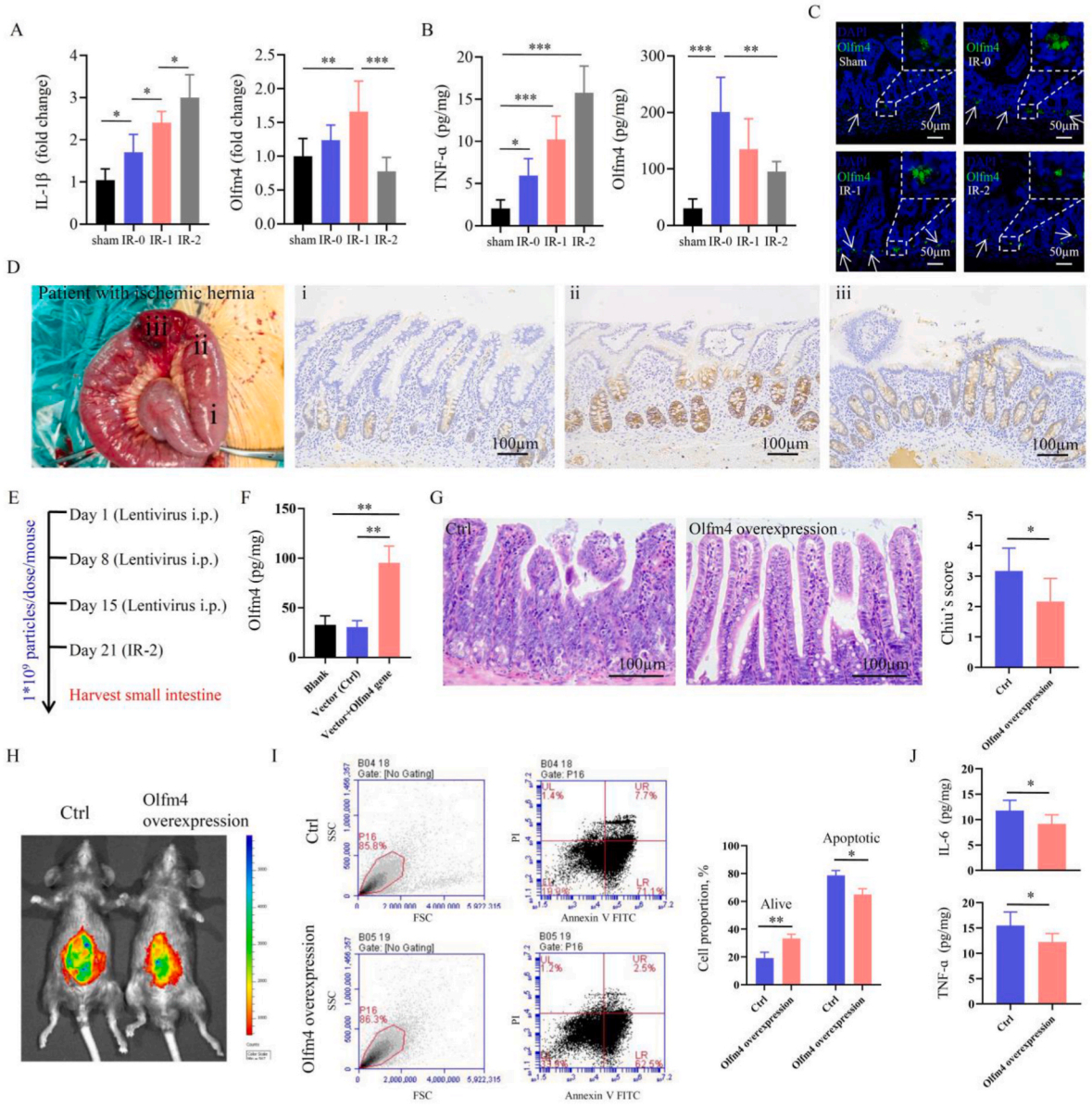

Fig. 8. Dynamic changes and functions of OLFM4 during intestinal IR injury *in vivo*. (A) The transcriptional changes of the pro-inflammatory cytokine (*IL-1β*) and *Olfm4* at the different time points of intestinal IR injury, n = 6. IR-0, -1, or -2 means 30-min ischemia followed by 0, 1, or 2-h reperfusion. (B) The protein levels of the pro-inflammatory cytokine (TNF-α) and OLFM4 at the different time points of intestinal IR injury, n = 6. (C) The change of *Olfm4* RNA was observed by fluorescence in situ hybridization in intestinal tissues at the different time points of intestinal IR injury. The arrows label the positively stained cells. (D) The relation of OLFM4 with spatially different extents of intestinal damage in the patient with an ischemic incisional hernia. i, mild lesion; ii, moderate lesion; and iii, severe lesion. (E) The protocol on the lentivirus transduction of mice. i.p., intraperitoneal injection. (F) The lentivirus increased the expression of *Olfm4* in the small intestine with *Olfm4* transcript, n = 3. (G) The representative HE staining images and Chiu's score of small intestinal samples following IR-2 injury in mice treated with vector lentivirus or the lentivirus with olfm4 transcript, n = 6. (H) The representative *in vivo* imaging pictures of MPO production by an MPO inflammation probe following IR-2 injury in mice treated with vector lentivirus or the lentivirus with *Olfm4* transcript. (I) The representative flow cytometry images and quantitative analysis on the measurement of small intestinal apoptotic cells following IR-2 injury in mice treated with vector lentivirus or the lentivirus with *Olfm4* transcript, n = 3. (J) The comparison of pro-inflammatory cytokine production (e.g., IL-6 and TNF-α) following IR-2 injury in mice treated with vector lentivirus or the lentivirus with *Olfm4* transcript, n = 6. *p < 0.05; **p < 0.01; ***p < 0.001.

damages (Fig. 8E). It was measured that the concentration of the *Olfm4* transcript in the small intestine of mice treated with lentivirus vector + *Olfm4* transcript was increased almost three times compared to the vector only-treated mice (Fig. 8F). After intervening with IR-2, the small intestine of mice with *Olfm4* overexpression presented less intestinal damage and lower Chiu's score than vector-only-treated mice (Fig. 8G, Fig. S14E). Moreover, *Olfm4* overexpression in the small intestine alleviated the production of myeloperoxidase (MPO) detected by *in vivo* imaging with an MPO inflammation probe (Fig. 8H, Fig. S14F), and improved the cell apoptosis (Fig. 8I). Meanwhile, the generation of pro-inflammatory cytokines (e.g., IL-6 and TNF-α) was reduced when the exhaustion of OLFM4 was improved (Fig. 8J). To this end, OLFM4 was validated to be an effective drug target for treating intestinal IR injury, and this discovery was due to the use of the highly biomimetic cell model of a microfluidic intestinal organoid-on-a-chip featuring on the recapitulation of oxygen dynamics during the intestinal IR injury.

3. Discussion

In this study, we presented a microfluidic intestinal organoid-on-a-chip model that allowed ultrafast change of the oxygen environment to simulate IR injury for the first time. Although the intestinal organoid model has recapitulated almost all intestinal epithelial cell types and their genetic signatures, the lack of perfusable physiological channels such as tubular digestive tract and nourished blood vessels inevitably leads to the uncontrollability of self-renewal, mechanical stimulation, and nutrient supply. Engineers are beginning to harness organoid-on-a-chip techniques to address partial complex intestinal microenvironments. A representative example can be found in a microfluidic intestinal chip by inducing intestinal stem cells to form tube-shaped epithelia with an accessible lumen to facilitate cell renewal and disease modeling of parasite infections [14]. However, some intestinal diseases are featured by interactions with extra-gut systems such as enteroplegia with disordered neuronal and glial cells in the nerve system [25], and intestinal IR injury with obstructive blood vessels in the circulatory system. Therefore, an organoid-on-a-chip is needed to achieve multi-organ interactions.

Excitingly, our chip has expanded the bio-responsiveness of intestinal organoids to extra-gut artificial vessels and created a biomimetic intestinal IR injury model featuring on fast HR dynamics [26]. The fabrication of the artificial vessels is based on the pH-sensitivity of ZIF-8 that releases zinc ions for crosslinking with SA through a convenient pH adjustment. Outside the sensitive pH ranges, ZIF-8 presents enough stability when blended with anionic polymers. This effect is first termed as "MOF-mediated ionic barrier" by the authors and enables to make a prepared commercial "vessel scaffold" kit for the artificial microvessels embedded in the organoid-on-a-chip. Moreover, owing to the artificial vessels, an eight-time increase in efficacy to reach equivalent hypoxia was achieved compared with a tri-gas incubator due to rapid oxygen diffusion in the liquid-to-liquid interface. Such a fast oxygen dynamic pattern is similar to that *in vivo* intestinal ischemia and facilitates the discovery of determinant molecules for IR injury [27–30]; otherwise, a delayed oxygen decline by using a tri-gas incubator may induce the adaption to hypoxia in mammals and cover up the discovery through reshaping molecular characteristics [31].

In combination with high-throughput sequencing with an organoid-on-a-chip, molecular mapping can be used to identify genes of interest. Herein, we found that rapid HR could lead to a significant decrease of *Olfm4* expression. OLFM4 was first cloned from granulocyte colony-stimulating factor-induced human myoblasts and mapped to chromosome 13q14.3 [32]. Regarding the inflammatory regulatory functions of OLFM4 in the intestinal system, recent investigations using *Olfm4*-deficient mice have provided important clues. Specifically, the mice with *Olfm4* deficiency exhibited robust inflammatory responses to bacterial infections and azoxymethane/dextran sodium sulfate-induced intestinal barrier damages [33]. Consistently, our study revealed that OLFM4 could reduce HR-triggered cellular inflammation by inhibiting the activation of NF-kappa B signaling. In mice with intestinal IR injury, the decreasing trend of OLFM4 at the late stage contributed to the exacerbation of intestinal inflammatory damages by unlocking the inhibition of NF-kappa B signaling. Once *Olfm4* is overexpressed from a lentivirus, intestinal damage can be relieved. However, OLFM4 was increased at the beginning of IR injury or in the mild lesion of the patient, which could exert transient protective functions in the context of intestinal IR injury. This paradoxical alteration of OLFM4 is possibly due to the existence of a feedback loop that NF-kappa B signaling also regulates *Olfm4* expression by binding to a DNA fragment corresponding to the −86 to −67 sequence of the *Olfm4* promoter [34,35]. However, regarding the role of OLFM4 in the extra-gut system, it is quite different from the findings in gut. For example, it was reported that OLFM4-positive neutrophils could lead to intestinal damages, and the deletion of OLFM4-positive neutrophils would relieve intestinal IR injury [36]. Overall, these studies remind us that the therapeutic purpose of the OLFM4 molecular target to improve intestinal IR injury outcome should be varied by the cell types.

Moreover, OLFM4 is a marker of ISCs and reflects stemness [37]. To our knowledge, the period of a physiological renewal of intestinal epithelia takes 3–5 days, starting with the death and detachment of absorptive cells followed by proliferation and differentiation of ISCs [38]. Therefore, during intestinal IR injury, the impairment of *Olfm4* expression implies the dysfunction of ISCs and failure in intestinal regeneration, thus losing the integrity of the intestinal structure and initiating a multi-factorial damage phase involved with bacterial translocation and immune cell infiltration. Altogether, we believe that the exhaustion of OLFM4 is a contributing cause of intestinal damage during IR injury, and OLFM4 can be a therapeutic molecular target.

4. Conclusion

This work first reported the manufacturing process of a microfluidic intestinal organoid-on-a-chip embedded with artificial microvessels, and addressed its application on extra-gut diseases. Specifically, this chip can recapitulate the features of *in vivo* intestinal tissues and IR injury in the following three aspects: (1) for biology, the use of intestinal organoids achieves full participation of intestinal epithelial cells under pathophysiological conditions; (2) for structure, the adjacent relationship of artificial microvessels and intestinal organoid is the same as the natural structure of intestinal villi that a central capillary is wrapped by surrounding intestinal epithelia and nourishes them; and (3) for oxygen dynamics, liquid-to-liquid gas diffusion enables rapid HR and prevents unintended shifts of the molecular map by mammals' intrinsic adaptive hypoxia competence. Supported by this technology, *Olfm4* is found for the first time to be the most significantly down-regulated gene in HR-treated intestinal organoids after RNA-sequencing. Furthermore, this gene encodes the OLFM4 protein, which can inhibit the activation of NF-kappa B signaling and reduce intestinal inflammation, thus allowing it to be a therapeutic target. Overall, our study offers a next-generation and highly biomimetic organoid-on-a-chip model to uncover molecular targets for some complex diseases involving multisystem interactions.

5. Materials and methods

5.1. Synthesis of ZIF-8 nanocrystals

ZIF-8 nanocrystals were synthesized in an aqueous solution using a classical hydrothermal synthesis following slightly modified instructions reported elsewhere [39,40]. First, 1.17 g of $Zn(NO_3)_2 \bullet 6H_2O$ (Sigma-Aldrich) and 22.70 g of 2-methylimidazole (Sigma-Aldrich) were dissolved in 40 mL of deionized (DI) water. To ensure that the mixing ligand solution could be fully dissolved, the solution was placed in an ultrasonic environment for 10 min until the solution became clear. Then, the metal solution was added to the resultant faint yellow ligand

solution with mild stirring at 30 °C for another 10 h. After that, the obtained white colloid was collected by centrifuging at 10,000 rpm for 10 min and alternately washed with DI water and fresh methanol three times. Finally, the resultant ZIF-8 nanocrystals were dried at 60 °C for future use. The morphology of ZIF-8 was observed with SEM (S-4800, Hitachi). The crystal structure was characterized by XRD (D8 Advance, Bruker). The concentration of Zn^{2+} in the supernatant of ZIF-8 solution was quantified with an atomic absorption spectrometer (Analytik Jena AG).

5.2. Fabrication and characterization of ZIF-8/SA scaffold

The crosslinking of ZIF-8/SA was based on pH sensitivity. Briefly, the ZIF-8 aqueous solution (2, 4, and 6 mg/mL) was homogeneously mixed with SA at the concentration of 2, 3, and 4 wt% and then adjusted to pH = 1 with a hydrochloric acid solution. The lysis of ZIF-8 crystals and emerging reactions with SA were confirmed using XRD and FTIR (Nicolet-6700, Thermo), respectively. The microstructure was observed with an SEM. Moreover, the solidification of hydrogel was validated with a rheometer (Anton Paar) by the crossing of G′ and G" in an oscillatory time sweep mode (1.0 Hz; 1% strain). The G′ and G" of resultant hydrogels were tested in an oscillatory frequency sweep mode (0.1–100 Hz; 1% strain). However, at pH = 7, ZIF-8/SA mixing solution would not be solidified by a one-year observation using a vial tilting method. In addition, the compressive strength of crosslinked hydrogel was measured with a universal testing machine (MTS CMT2103, USA). The toughness (T) was calculated using Eqn. (1) based on the integral of the area under the compressive stress (τ)-strain (ε) curve:

$$T = \int \tau d\varepsilon. \quad (1)$$

5.3. Construction of hollow structure

The shear-thinning property of the ZIF-8/SA precursor solution was verified in a viscosity mode at shear rates from 0.5 to 100 s^{-1}, which allowed it to be manufactured with the hollow structure using the extrusion-based co-axial microfluidic equipment [41]. The inner nozzle was fused with a hydrochloric acid solution, and the outer nozzle was fused with ZIF-8/SA mixing solution. By adjusting the nozzle diameter and flow rate, the regulatory performance in the size of hollow fibers could be observed with a light microscope (XD-202, NOVEL). In addition, the hollow structure of the hydrogel fibers was revealed using an SEM. The obtained hollow fibers were treated with phosphate buffer solution (PBS, KeyGEN Biotech, China) to neutralize the acidity before fabricating artificial microvessels.

5.4. Fabrication and characterization of artificial microvessels

We constructed bio-interfaces on the inner surface of hollow fibers by intraluminal injection of 20 v/v% Matrigel (Corning, USA) to enhance cell adhesion and spread. Then, 1×10^6/mL of HUVECs (P2-P4, Sciencell, USA) culture in ECM medium (Sciencell, USA) was transfused into the entire lumen. The morphological alteration of HUVECs in the hollow fiber was observed with the light microscope. Moreover, according to the manufacturer's instructions, the cell survival was detected with a live/dead kit (KeyGEN Biotech, China), the cell proliferation was measured with a CCK-8 kit (Servicebio, China), and the cells were re-identified with a vascular endothelial marker (CD31) and a cytoskeleton marker (F-actin) using the CD31 antibody (Table S3) and Alexa Fluor™ Plus 555 (Invitrogen, USA), respectively.

Moreover, the physical properties of the artificial vessels were characterized in terms of permeability, elasticity, and blood pressure tolerance. To visualize the permeability, we injected 1% acid blue (Aladdin) aqueous solution into the lumen of hollow fiber and sealed the fiber by tying a knot on the two ends. Moreover, we compared the permeation speed of dyes with different molecule weights using low molecular weight FITC (0.1 mg/mL, MKbio, China) and high molecular weight BSA-FITC (15 v/v%, Bersee Biotech, China). The permeation process through the wall of hollow fibers could be observed using a confocal microscope (ZEISS, LSM 980). The permeated dyes were quantitatively detected with a multi-functional microplate reader (Bio-Tek) at the absorbance of 495 nm. The proportion of release was calculated by the ratio of permeated dyes to the total amount of dyes at preset time points (0, 80, 160, 240, 320, and 400 min). The elasticity was evaluated by stretching the artificial vessels and quantitatively measuring with the universal testing machine (MTS, CMT2103, USA). Finally, the blood pressure tolerance was defined as the maximal value recorded by a digital manometer (AZ Instrument, 8205) when continuously inflating the hollow fiber.

5.5. ISC-derived intestinal organoid culture

ISCs were isolated from 4-week-old C57BL/6 mice by referring to the previous protocol with slight modifications [11], and the Animal Ethics Committee of Jingling Hospital approved the animal ethics (2021DZDWLS-001). The small intestine was harvested and intraluminally rinsed with cold PBS to remove intestinal contents. Then, the intestinal wall was cut off longitudinally and softly scraped with a throat swab to remove residual mucus and potential contaminations, followed by separation into small pieces with 2–3 mm in width collected in a 50-mL Falcon tube filled with 20 mL PBS containing 5 mM EDTA. The tube was then rotated at 4 °C for 40 min. Vigorous handshaking was used to dissociate crypts containing ISCs, and a 70-μm cell strainer was applied to purify the crypts. Subsequently, the crypts were mixed with diluted Matrigel (70 v/v%) at a density of 1,500 per 50 μL gel, and 40 μL drops of Matrigel-crypt suspension were spotted into wells of 24 well plate. After gel solidification, complete organoid medium was added, which consisted of advanced DMEM/F12 containing 15% fetal bovine serum (KeyGEN Biotech, China), 1% penicillin/streptomycin (KeyGEN Biotech, China), 50 ng/mL EGF (PeproTech, USA), 100 ng/mL Noggin (PeproTech, USA), and 250 ng/mL R–spondin (PeproTech, USA). The medium was changed every 3–4 days. Organoids were passaged every 6–8 days. Cell recovery solution (Corning, USA) at 4 °C was used to dissolve Matrigel.

5.6. Development of microfluidic intestinal organoid-on-a-chip embedded with artificial vessels

The chip was fabricated through replicating a male PMMA model with PDMS. The male model was designed with SOLIDWORKS software and machined on PMMA with a CNC router. It was constituted with upper and lower templates with five semi-cylindrical channels (0.6 mm in radius) in each template, as shown in Fig. S10A. On this basis, four semi-cylindrical chambers (2.6 mm in radius, 2 mm in height) along the channels were additionally constructed at the interval distance of 5 mm in one template. Afterward, PDMS (Dow Corning 184) at a weight ratio of 10:1 was prepared by stirring and removing air bubbles in a vacuum box and poured in the PMMA mold. After curing in a 60 °C drying oven for 4 h, we obtained the PDMS cover and bottom of the chip. The prepared artificial vessels were laden onto the semi-cylindrical channels, and then intestinal organoid-complete organoid medium (30 v/v %)-Matrigel (70 v/v%) suspension at the density of 30 per 20 μL gel was added into the chamber (20 μL in volume). The microfluidic pump was used to perfuse different culture media (e.g., normal organoid medium, hypoxic organoid medium, and organoid medium with 500 μM hydrogen peroxide) into the artificial vessels at the rate of 0.5 mL/h. To monitor the ROS production, the ROS fluorescent probe 2,7-dichlorodihydrofluorescein diacetate (DCFH-DA) was pre-loaded in Matrigel at the concentration of 10 μM, and then imaged with a chemiluminescent imaging system (Tanon, China) at 488 nm.

5.7. Simulation and validation of oxygen dynamics

A finite element method based on COMSOL Multiphysics 5.6 (COMSOL Inc.) was used to predict the oxygen concentration of intestinal organoid-embedded Matrigel in the chip. To compute the process, transport of diluted species with the time-dependent study was used according to Fick's second law, as seen in Eqn (2):

$$\frac{\partial c_i}{\partial t} + \nabla \bullet J_i + u \bullet \nabla c_i = R_i, \quad (2)$$

where $J_i = -D_i \nabla c_i$; c, concentration (mol/m^3); t, time (s); J, flux (mol/m^2s); u, flow velocity (m/s); R, volumetric rate of reaction (mol/m^3s); and D, diffusion coefficient (m^2/s). The flow channel of culture medium, artificial vessel, and Matrigel-embedded chamber were drawn based on the actual dimensions. The constants used in the COMSOL simulation were listed in Tables S1 and S2, in which the oxygen diffusion coefficients in the culture medium, artificial vessel, and Matrigel were 2.7 $\times 10^{-9}$ m^2/s, 1.8 $\times 10^{-9}$ m^2/s, and 1.7 $\times 10^{-9}$ m^2/s, respectively [42,43]. To confirm the simulation results, the oxygen concentration in the chip was measured with an oxygen meter (Leici, China).

5.8. Immunofluorescence assay of intestinal organoids

Immunofluorescence staining of intestinal organoids was conducted based a reported protocol with slight modifications [44]. Briefly, intestinal organoids were isolated by manual disruption and fixed in a 4% paraformaldehyde solution. After a complete PBS wash, organoid wash buffer prepared by adding 1 mL Triton X–100 and 2 g BSA to 1 L PBS was added to block and permeabilize organoids. Then, the organoids were incubated with the staining TUNEL reagent (KeyGEN Biotech, China) or the primary antibodies such as β-Catenin (mainly located in the cell membrane for Wnt signaling transduction), Ki-67 (cell proliferation), ZO-1 (intercellular tight junction), Villin (the major component of microvilli of intestinal epithelial cells) followed by secondary antibodies listed in Table S3. Finally, the stained organoids were imaged with confocal microscopy.

5.9. RNA isolation, sequencing, and PCR

Total mRNA samples of intestinal organoids were extracted by TRIzol (Sigma-Aldrich). Sequencing libraries were constructed using NEBNext® Ultra™ RNA Library Prep Kit following the manufacturer's instructions, and index codes were added to attribute sequences to each sample. RNA concentration of the library was validated using Qubit® RNA Assay Kit in Qubit® 3.0 and then diluted to 1 ng/μL. Insert size was assessed with Agilent Bioanalyzer 2100 system (Agilent Technologies, USA) and also accurately quantified with StepOnePlus™ Real-Time PCR System (concentration >10 nM). The cluster generation and sequencing were performed on NovaSeq 6000 S4 platform, using NovaSeq 6000 S4 Reagent kit V1.5. The gene differential expression analysis was based on the R package DESeq2, in which genes with $\log_2$(fold change) > 1 were considered statistically significantly different. Enrichment analysis was conducted for all of the genes mapped with the KEGG database. RNA-sequencing data were deposited in the SRA database (accession No. PRJNA810577).

Real-time PCR was performed according to our regular protocol [45]. Briefly, after total RNA was extracted, it was reverse-transcribed with HiScript III RT SuperMix (Vazyme Biotech, China). According to the manufacturer's instructions, the reverse transcription products were then amplified by QuantStudio™ 3 (Applied Biosystems) using SYBR Green QPCR Master Mix (Vazyme Biotech, China). The relevant primer sequences are listed in Table S4. Finally, all of the data of mRNA expression were normalized to β-actin.

5.10. Detection of oxidative stress and cytokines

Commercial kits were used to measure the concentrations of SOD (KGT00150, KeyGen Biotech), MDA (KGT003, KeyGen Biotech), human IL-1β (CSB-E08053h, Cusabio), human TNF-α (88-7346-88, Invitrogen), mouse TNF-α (88-7324, Invitrogen), mouse IL-6 (88-7064, Invitrogen), and mouse OLFM4 (EM1252, Fine Biotech) in the indicated samples according to each manufacturer's instructions.

5.11. Western blot

Cells were lysed in RIPA lysis buffer (P0013B, Beyotime) with protease inhibitor cocktail (HY-K0010, MCE), PMSF (ST506, Beyotime), and phosphatase inhibitor cocktail (HY-K0021, MCE) for 20 min on ice. The lysates were centrifuged at 14,000 g at 4 °C for 15 min, and the supernatants were boiled for 10 min after being mixed with SDS loading buffer. Proteins were separated by sodium dodecyl sulfate-polyacrylamide gel electrophoresis (SDS-PAGE) and transferred onto a polyvinylidene fluoride membrane (Millipore). After blocking with 5 wt % milk-contained Tris-buffered saline Tween 20 (TBST), the membrane was incubated overnight with the intended primary antibody at 4 °C. Next day, the membrane was washed with TBST and incubated with a secondary antibody for 1 h at room temperature. The antibody information was also given in Table S3. Finally, the blots were imaged using the Tanon chemiluminescent imaging system.

5.12. Lentivirus-mediated transduction of intestinal organoids

The composition of lentivirus particles for *Olfm4* interference or *Olfm4* overexpression was presented in Fig. S12, and SyngenTech produced them at the concentration of 2–3 $\times 10^8$ TU/mL. The procedures for lentivirus transduction on intestinal organoids were as previously described [46]. As shown in Fig. 7A, before using lentivirus, the mature intestinal organoids were pretreated with the supplement organoid culture medium with 10 μM Chir99021 (HY-10182, MCE) and 10 mM nicotinamide (HY-B0150, MCE) to obtain cystic hyperproliferative crypts. Then, the organoid-embedded domes were disrupted with a micropipette, and then the organoid was separated from the mixture by centrifugation at 100×*g* and treated with 0.25% trypsin for 3min at 37 °C. Subsequently, the trypsin was inactivated, and the organoids were centrifuged. The pellet was collected in a well of a 24-well plate followed by adding 500 μL complete organoid medium with 4–8 μL of 1 $\times 10^8$ TU/mL lentivirus particles. The mixture was then resuspended and incubated at 37 °C for 2 h, followed by an additional 1 h of spinoculation. The mixture was then centrifuged, and the pellet was resuspended in Matrigel domes and cultured in the organoid culture medium supplemented with 10 mM nicotinamide, 10 μM Chir99021, and 10 μM Y27632 (HY-10071, MCE). Three days later, the lentivirus-infected organoids were confirmed with green fluorescence under confocal microscopy and grown under puromycin positive selection. For organoid maturation and later intended experiments, the survived cells were resuspended in Matrigel domes.

5.13. Preparation of OLFM4-loaded liposome

First, 10 mg 1,2-Distearoyl-sn-glycerol-3-phosphocholine (L130335, Aladdin) and 1 mg cholesterol (C104032, Aladdin) were dissolved in ethanol and added into a 25-mL eggplant-shaped flask to form a film by rotary evaporation in a vacuum dryer for 2 h. Then, 1 mL PBS with 12.5 μg OLFM4 recombinant protein (HY-P71179, MCE) was added to the flask filled with nitrogen and treated with 60 min of hydration by shaking and 5 min of ultrasonication in a water bath. In this way, OLFM4-loaded liposome was prepared and then collected at 4 °C for use.

5.14. Intestinal IR injury in mice

Wild-type C57BL/6 J mice (8–12 weeks) were purchased from Huachuang Sino Co., Ltd. All of the mice were housed in individual cages with controlled temperature and natural light-dark cycles. The Animal Investigation Ethics Committee of Jinling Hospital approved this animal protocol (2021DZDWLS-001). Intraperitoneal injection of lentivirus at 1×10^9 copies/week for three weeks was used to construct *Olfm4*-overexpressed mice [47]. The lentivirus without *Olfm4* transcript was the vector control.

Mice were anesthetized intraperitoneally with pentobarbital (50 mg/kg). Then, a midline laparotomy was conducted. The superior mesenteric artery was separated and occluded with a microvascular clamp for 30 min followed by the clamp removal for a period of reperfusion time.

5.15. Patients with intestinal ischemia

A patient with an incisional hernia was prospectively enrolled. The patient was confirmed in surgery with different intestinal ischemia conditions in varying locations. Intestinal biopsy was performed in these locations to investigate the relation of intestinal ischemia severity with *Olfm4* expression. The Clinical Ethics Committee of Jinling Hospital approved this protocol (No. 2022NZKY-010-01), and informed consent was obtained.

5.16. Histological analysis

Small intestine samples were harvested at 0, 1, and 2 h after 30-min ischemia or from the mice of sham surgery, and then fixed in 4% paraformaldehyde. After being dehydrated in ethanol, the samples were embedded with paraffin and stained with hematoxylin and eosin (H&E). Chui's score system was used to evaluate intestinal injury [48].

For tissue immunohistochemistry, paraffin sections were deparaffinized with xylene and rehydrated with a concentration gradient of ethanol. Then, antigen retrieval by using a microwave oven was performed, and the samples were incubated with the intended primary antibodies and secondary antibodies (listed in Table S3) and reacted with DAB color developing solution (Servicebio, China) and hematoxylin stain solution (Servicebio, China). Afterward, the sections were rinsed, dehydrated, cleared, and mounted. The recorded images were quantified with ImageJ (NIH, USA).

For tissue immunofluorescence staining, paraffin sections were deparaffinized with xylene and rehydrated with a concentration gradient of ethanol. Then, antigen retrieval was performed, and the samples were incubated with intended primary antibodies and secondary antibodies (listed in Table S3) and reacted with DAPI (Servicebio, China). After quenched intrinsic fluorescence was performed with a kit (G1221-5 ML, ServiceBio, China) and samples were mounted, they were imaged with a fluorescence microscope (Nikon Eclipse C1).

For tissue fluorescence in situ hybridization of *Olfm4* RNA, paraffin sections were deparaffinized with xylene and rehydrated with a concentrated gradient of ethanol. The samples were digested with 20 μg/ml proteinase K (Servicebio, China) at 37 °C for 20 min and then incubated with 1 μM *Olfm4* probe at 42 °C overnight. The probe is described as:

5′-FAM-GAAGCGAUUAUUGUAGGCAGCCAGAGGGAG-FAM-3'.

After removing the probe and staining with DAPI, the images of samples were obtained using a fluorescence microscope.

5.17. In vivo imaging

Intestinal inflammation was evaluated by XenoLight RediJect Inflammation Probe (PerkinElmer) using an IVIS imaging system (XRMS Serise III). This probe was sensitive to myeloperoxidase production. Specifically, 150 μL of 40 mg/mL probe was injected intraperitoneally 5 min before imaging, and bioluminescence signals in regions of interest were recorded and quantified.

5.18. Flow cytometry of intestinal cell apoptosis

The fresh intestinal tissue was stored in tissue preservation solution (Singleron, China) and digested with 2 mL tissue dissociation solution (Singleron) at 37 °C for 15 min in 15 ml centrifuge tube with sustained agitation. After that, the samples were filtered using 40-μm sterile strainers to obtain cell suspension. First, red blood cell lysis buffer (Singleron) removed red blood cells. Then, the cell suspension was stained using a cell apoptosis kit (Beyotime Biotech, China) and analyzed with a flow cytometer (BD ACCURI C6 PLUS).

5.19. Statistics

Data were analyzed using GraphPad Prism 8.2.1 software by Student's t-test (unpaired and two-tailed) or one-way ANOVA (analysis of variance). Multiple comparisons were conducted if needed. The survival curve depicted the survival of mice. The values were considered significantly different when $p < 0.05$.

Ethics approval and consent to participate

The Animal Ethics Committee of Jingling Hospital approved the animal ethics (2021DZDWLS-001). The Clinical Ethics Committee of Jinling Hospital approved the acquisition and use of postoperative intestinal samples of patients (No. 2022NZKY-010-01), and informed consent was obtained.

Funding

This study is funded by the National Natural Science Foundation of China (82270595, 82272237, 82072223, 32171402), the China Postdoctoral Science Foundation (BX20220393, 2022M723891), the General Program of Medical Research from the Jiangsu Commission of Health (M2020052), the Jiangsu Key Research and Development Plan (BE2021727), and Jiangsu Provincial Medical Innovation Center (CXZX202217).

Data and materials availability

Key data needed to evaluate the conclusions are present in the paper and/or the Supplementary Materials. The processed data of RNA sequencing including the gene name, expression differences, and functional annotations were available via an external link: https://pan.baidu.com/s/1TX36Vk8IUZGw0prG94Ahdw?pwd=fx21. Raw images of western blot were uploaded in Supplementary File. The other data of interests will be available upon e-mail request.

CRediT authorship contribution statement

Jinjian Huang: Conceptualization, Funding acquisition, Investigation, Methodology, Software, Writing – original draft, Writing – review & editing. **Ziyan Xu:** Investigation. **Jiao Jiao:** Investigation. **Zongan Li:** Funding acquisition, Methodology, Software. **Sicheng Li:** Investigation. **Ye Liu:** Investigation. **Ze Li:** Investigation. **Guiwen Qu:** Investigation. **Jie Wu:** Investigation. **Yun Zhao:** Investigation. **Kang Chen:** Investigation. **Jieshou Li:** Supervision, Validation. **Yichang Pan:** Conceptualization, Supervision, Validation. **Xiuwen Wu:** Conceptualization, Funding acquisition, Supervision, Validation, Writing – review & editing. **Jianan Ren:** Conceptualization, Funding acquisition, Supervision, Validation.

Declaration of competing interest

The authors declare that they do not have any competing interests.

Acknowledgment

We thank Yang Liu at China Pharmaceutical University for his contribution to developing the OLFM4-loaded liposome, and Kang Yang at Anoroad Gene Technology Co., Ltd. for his assistance in RNA sequencing.

Appendix A. Supplementary data

Supplementary data to this article can be found online at https://doi.org/10.1016/j.bioactmat.2023.07.001.

References

[1] T. Kalogeris, C.P. Baines, M. Krenz, R.J. Korthuis, Ischemia/reperfusion, Compr. Physiol. 7 (2016) 113–170.
[2] M. Stamatakos, C. Stefanaki, D. Mastrokalos, et al., Mesenteric ischemia: still a deadly puzzle for the medical community, Tohoku J. Exp. Med. 216 (2008) 197–204.
[3] J. Grootjans, K. Lenaerts, W.A. Buurman, et al., Life and death at the mucosal-luminal interface: new perspectives on human intestinal ischemia-reperfusion, World J. Gastroenterol. 22 (2016) 2760–2770.
[4] Y. Li, D. Feng, Z. Wang, et al., Ischemia-induced ACSL4 activation contributes to ferroptosis-mediated tissue injury in intestinal ischemia/reperfusion, Cell Death Differ. 26 (2019) 2284–2299.
[5] D. Newby, L. Marks, F. Lyall, Dissolved oxygen concentration in culture medium: assumptions and pitfalls, Placenta 26 (2005) 353–357.
[6] J. Grootjans, K. Lenaerts, J.P. Derikx, et al., Human intestinal ischemia-reperfusion-induced inflammation characterized: experiences from a new translational model, Am. J. Pathol. 176 (2010) 2283–2291.
[7] C.B. Thompson, Into thin air: how we sense and respond to hypoxia, Cell 167 (2016) 9–11.
[8] M. Serocki, S. Bartoszewska, A. Janaszak-Jasiecka, et al., miRNAs regulate the HIF switch during hypoxia: a novel therapeutic target, Angiogenesis 21 (2018) 183–202.
[9] J. Xin, H. Zhang, Y. He, et al., Chromatin accessibility landscape and regulatory network of high-altitude hypoxia adaptation, Nat. Commun. 11 (2020) 4928.
[10] Y. Peng, C. Cui, Y. He, et al., Down-regulation of EPAS1 transcription and genetic adaptation of Tibetans to high-altitude hypoxia, Mol. Biol. Evol. 34 (2017) 818–830.
[11] T. Sato, R.G. Vries, H.J. Snippert, et al., Single Lgr5 stem cells build crypt-villus structures in vitro without a mesenchymal niche, Nature 459 (2009) 262–265.
[12] J. Huang, Y. Ren, X. Wu, et al., Gut bioengineering promotes gut repair and pharmaceutical research: a review, J. Tissue Eng. 10 (2019), 1013333264.
[13] H. Yan, H.C. Siu, S. Law, et al., A comprehensive human gastric cancer organoid biobank captures tumor subtype heterogeneity and enables therapeutic screening, Cell Stem Cell 23 (2018) 882–897.
[14] M. Nikolaev, O. Mitrofanova, N. Broguiere, et al., Homeostatic mini-intestines through scaffold-guided organoid morphogenesis, Nature 585 (2020) 574–578.
[15] W. Shin, C.D. Hinojosa, D.E. Ingber, H.J. Kim, Human intestinal morphogenesis controlled by transepithelial morphogen gradient and flow-dependent physical cues in a microengineered gut-on-a-chip, iScience 15 (2019) 391–406.
[16] S.E. Park, A. Georgescu, D. Huh, Organoids-on-a-chip, Science 364 (2019) 960–965.
[17] C. Hans, L. Madeline, Takanori, Advances in organoid technology: hans clevers, madeline lancaster, and takanori takebe, Cell Stem Cell 20 (2017) 759–762.
[18] R. Sabater I Serra, J. Molina-Mateo, C. Torregrosa-Cabanilles, et al., Bio-nanocomposite hydrogel based on zinc alginate/graphene oxide: morphology, structural conformation, thermal behavior/degradation, and dielectric properties, Polymers 12 (2020) 702.
[19] A.J. Howarth, Y. Liu, P. Li, et al., Chemical, thermal and mechanical stabilities of metal–organic frameworks, Nat. Rev. Mater. 1 (2016), 15018.
[20] J. Jiao, F. Wang, J. Huang, et al., Microfluidic hollow fiber with improved stiffness repairs peripheral nerve injury through non-invasive electromagnetic induction and controlled release of NGF, Chem. Eng. J. 426 (2021), 131826.
[21] R.B. Hamanaka, S.E. Weinberg, C.R. Reczek, N.S. Chandel, The mitochondrial respiratory chain is required for organismal adaptation to hypoxia, Cell Rep. 15 (2016) 451–459.
[22] M. Dostalek, K.D. Hardy, G.L. Milne, et al., Development of oxidative stress by cytochrome P450 induction in rodents is selective for barbiturates and related to loss of pyridine nucleotide-dependent protective systems, J. Biol. Chem. 283 (2008) 17147–17157.
[23] W. Liu, M. Yan, Y. Liu, et al., Olfactomedin 4 down-regulates innate immunity against Helicobacter pylori infection, P NATL ACAD SCI USA 107 (2010) 11056–11061.
[24] L. Chen, R.P. Vasoya, N.H. Toke, et al., HNF4 regulates fatty acid oxidation and is required for renewal of intestinal stem cells in mice, Gastroenterology 158 (2020) 985–999.
[25] D.F. Chang, S.M. Zuber, E.A. Gilliam, et al., Induced pluripotent stem cell-derived enteric neural crest cells repopulate human aganglionic tissue-engineered intestine to form key components of the enteric nervous system, J. Tissue Eng. 11 (2020), 1542332187.
[26] A.M. Kip, Z. Soons, R. Mohren, et al., Proteomics analysis of human intestinal organoids during hypoxia and reoxygenation as a model to study ischemia-reperfusion injury, Cell Death Dis. 12 (2021) 95.
[27] M.G. McCabe, D.J. Maguire, R. Bourgain, The flux of oxygen within tissues, Adv. Exp. Med. Biol. 540 (2003) 291–295.
[28] K. Groebe, G. Thews, Basic mechanisms of diffusive and diffusion-related oxygen transport in biological systems: a review, Adv. Exp. Med. Biol. 317 (1992) 21–33.
[29] C.C. Hsia, A. Schmitz, M. Lambertz, et al., Evolution of air breathing: oxygen homeostasis and the transitions from water to land and sky, Compr. Physiol. 3 (2013) 849–915.
[30] A. Colom, R. Galgoczy, I. Almendros, et al., Oxygen diffusion and consumption in extracellular matrix gels: implications for designing three-dimensional cultures, J. Biomed. Mater. Res. A 102 (2014) 2776–2784.
[31] C. Michiels, Physiological and pathological responses to hypoxia, Am. J. Pathol. 164 (2004) 1875–1882.
[32] J. Zhang, W.L. Liu, D.C. Tang, et al., Identification and characterization of a novel member of olfactomedin-related protein family, hGC-1, expressed during myeloid lineage development, Gene 283 (2002) 83–93.
[33] W. Liu, G.P. Rodgers, Olfactomedin 4 expression and functions in innate immunity, inflammation, and cancer, CANCER METAST REV 35 (2016) 201–212.
[34] W. Liu, H.W. Lee, Y. Liu, et al., Olfactomedin 4 is a novel target gene of retinoic acids and 5-aza-2'-deoxycytidine involved in human myeloid leukemia cell growth, differentiation, and apoptosis, Blood 116 (2010) 4938–4947.
[35] K.L. Chin, W. Aerbajinai, J. Zhu, et al., The regulation of OLFM4 expression in myeloid precursor cells relies on NF-kappaB transcription factor, BRIT J HAEMATOL 143 (2008) 421–432.
[36] N.C. Levinsky, J. Mallela, A.M. Opoka, et al., The olfactomedin-4 positive neutrophil has a role in murine intestinal ischemia/reperfusion injury, Faseb. J. 33 (2019) 13660–13668.
[37] K. Suzuki, T. Murano, H. Shimizu, et al., Single cell analysis of Crohn's disease patient-derived small intestinal organoids reveals disease activity-dependent modification of stem cell properties, J. Gastroenterol. 53 (2018) 1035–1047.
[38] S. Asfaha, Intestinal stem cells and inflammation, Curr. Opin. Pharmacol. 25 (2015) 62–66.
[39] Y. Pan, Y. Liu, G. Zeng, et al., Rapid synthesis of zeolitic imidazolate framework-8 (ZIF-8) nanocrystals in an aqueous system, Chem. Commun. 47 (2011) 2071–2073.
[40] F. Yang, H. Mu, C. Wang, et al., Morphological map of ZIF-8 crystals with five distinctive shapes: feature of filler in mixed-matrix membranes on C3H6/C3H8 separation, Chem. Mater. 30 (2018) 3467–3473.
[41] J. Huang, Z. Li, Q. Hu, et al., Bioinspired anti-digestive hydrogels selected by a simulated gut microfluidic chip for closing gastrointestinal fistula, iScience 8 (2018) 40–48.
[42] D.A. Brown, W.R. Maclellan, H. Laks, et al., Analysis of oxygen transport in a diffusion-limited model of engineered heart tissue, Biotechnol. Bioeng. 97 (2010) 962–975.
[43] L. Figueiredo, R. Pace, C. D'Arros, et al., Assessing glucose and oxygen diffusion in hydrogels for the rational design of 3D stem cell scaffolds in regenerative medicine, J TISSUE ENG REGEN M 12 (2018) 1238–1246.
[44] J.F. Dekkers, M. Alieva, L.M. Wellens, et al., High-resolution 3D imaging of fixed and cleared organoids, Nat. Protoc. 14 (2019) 1756–1771.
[45] X. Zhang, J. Wu, Q. Liu, et al., mtDNA-STING pathway promotes necroptosis-dependent enterocyte injury in intestinal ischemia reperfusion, Cell Death Dis. 11 (2020) 1050.
[46] F. Jooske, Van, et al., A protocol for lentiviral transduction and downstream analysis of intestinal organoids, JoVE 98 (2015), e52531.
[47] S. Liu, Lentiviral-mediated systemic RNA interference in vivo, Methods Mol. Biol. 1868 (2018) 137–144.
[48] C.J. Chiu, A.H. McArdle, R. Brown, et al., Intestinal mucosal lesion in low-flow states. I. A morphological, hemodynamic, and metabolic reappraisal, Arch. Surg. 101 (1970) 478–483.